High-Throughput High-Resolution Digital Image Correlation Measurements by Multi-Beam SEM Imaging

R. L. Black[1] · T. Garbowski[2] · C. Bean[1] · A. L. Eberle[2] · S. Nickell[2] · D. Texier[3] · V. Valle[4] · J. C. Stinville[1]

Abstract

Background Recent improvements in spatial resolution and measurement sensitivity for high-resolution digital image correlation (HR-DIC) now provide an avenue for the quantitative measurement of deformation events and capturing the physical nature of deformation mechanisms. However, HR-DIC measurements require significant time due to scanning electron image acquisition; such a limitation prevents the widespread use of HR-DIC for material characterization.

Objective Apply a novel SEM acquisition technology to enhance HR-DIC measurements for high throughput applications.

Methods Multi-beam SEM technology is employed to image an entire gauge length at once at high resolution and at nearly a hundredfold acceleration of typical HR-DIC image acquisition, even when automated stage movement and image acquisition are employed. These images were fed into a discontinuity-tolerant HR-DIC software to determine slip localization induced by non-metallic inclusions and grain structure.

Results Slip localization was able to be analyzed to an unprecedented level, with over 210,000 slip bands able to be investigated, with the most intense slip localizing near and parallel to twin boundaries and in the vicinity of non-metallic inclusion clusters. Additionally, secondary slip activation and grain boundary shearing by intense dislocation pileups are observed to reduce slip amplitude near and parallel to twin boundaries.

Conclusions By performing HR-DIC in conjunction with a multi-beam SEM, high-throughput measurements of large field-of-view, high-resolution images were able to be performed in a timely manner. These measurements provided an immense number of slip events for statistical analysis to be performed on to relate to microstructural features.

Colorblind-friendly versions (protanopia, deuteranopia, tritanopia, and BGR-to-RBG) are provided in supplementary materials. Figures were generated using the Python Colorblind package version 0.0.9 and the ImageJ Simulate Color Blindness plug-in under the Image>Color menu (Wolfgang Rahfeldt 2021, Colorblind, Version 0.0.9. Retrieved from https://pypi.org/project/colorblind/ and J Schindelin et al, 2012, Fiji: an open-source platform for biological-image analysis, Nat Methods 9(7):676–682. https://doi.org/10.1038/nmeth.2019.)

✉ R. L. Black
rlb8@illinois.edu

[1] Materials Science and Engineering, University of Illinois at Urbana-Champaign, Champaign, USA

[2] Carl Zeiss MultiSEM GmbH, Oberkochen, Germany

[3] Institut Clément Ader (ICA), Université de Toulouse, CNRS, IMT Mines Albi, INSA, ISAE-SUPAERO, UPS, Campus Jarlard, Albi, France

[4] Institut PPRIME, Université de Poitiers, CNRS, ENSMA, Poitiers, France

Introduction

The recent emergence of integrated experimental tools that explicitly incorporate the physical nature of the deformation field at the nano-scale with representative fields of view at the millimeter scale now allows for new pathways to extract relationships between deformation fields and the structure and microstructure of materials. Experimental tools are, among others, high-resolution digital image correlation (HR-DIC) by scanning electron microscopy (SEM) [1], automated nano-indentation [2, 3], high-throughput mechanical testing of miniaturized speci-mens [4] and high-speed atomic force microscopy [5]. They all capture physical signatures of deformation processes. Moreover, they represent the complex microstructure of metallic materials by probing large surface or volume elements. Consequently, these experimental tools reveal the effect of microstructure heteroge-neity at the micro- and mesoscale on the deformation fields and

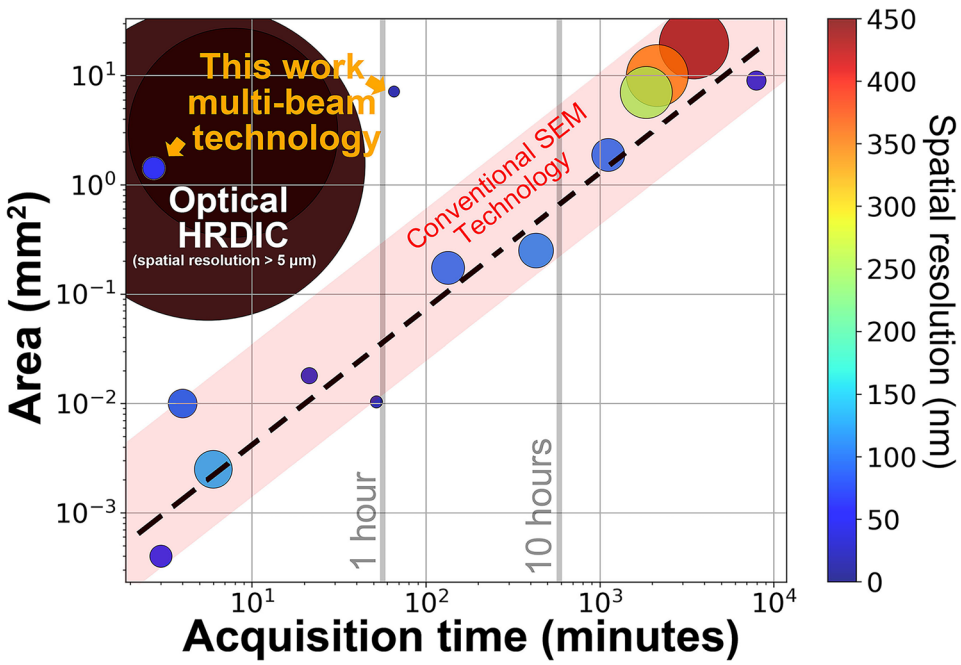

Fig. 1 Scanning electron microscopy for high-resolution digital image correlation. Investigated area as a function of HR-DIC images acquisition time to capture deformation processes in metallic materials: deformation slip [10, 15, 21–23, 25–31], grain boundary sliding [23], and deformation twin [19]. Data are extracted from recent literature. The size and color of the dot indicate the corresponding spatial resolution. As references, acquisition times and associated investigated surface areas from relevant studies using optical HR-DIC [28, 32, 33] are also provided. The present technology is used to accelerate HR-DIC measurements under SEM significantly

elucidate the link between the heterogeneous deformation, microstructure, and macroscopic mechanical behaviors. For instance, the relationship between nano-scale slip deformation in metallic materials and macroscopic properties such as fatigue strength has been demonstrated using high-resolution digital image correlation measurements inside an SEM over large fields of view [6].

HR-DIC by SEM is of great interest since it allows acquir-ing deformation data over large fields of view with spatial and displacement resolutions at the nano-scale [7, 8]. Digital image correlation (DIC) allows, by capturing images prior to and dur-ing loading, for the measurement of the displacement/defor-mation of a specimen subjected to mechanical loading. When imaging is performed with an SEM, nano-scale displacement resolution is obtained. In addition, complex loading conditions such as cyclic, biaxial, or high-temperature loading [10–12] can be applied, while HR-DIC can still be performed. Moreover, this technique is especially adapted for multi-modal and cor-relative measurements [12, 13] and dynamic measurements [14] allowing for microstructure-mechanical property relationship identification. Significant efforts in the past decade have been made to improve HR-DIC measurements. The development of robust nanometer-scale patterning techniques has significantly improved the reliability, sensitivity, and resolution of the HR-DIC measurements [16–18]. In parallel, the effect of scanning electron imaging on HR-DIC measurements has been detailed [17, 18] and SEM spatial and drift distortion minimized [14] to improve the resolution of the measurements. More recently, automation in image acquisition and mechanical testing [14] via scripting has facilitated the acquisition of HR-DIC meas-urements over a wide field of view. However, one of the main drawbacks of the HR-DIC measurements under SEM is the acquisition time. High-resolution SEM images over large fields of view are required to capture nano-scale displacements over regions that are representative of the microstructure of a material, making HR-DIC measurements very time-consuming. The typical acquisition times for HR-DIC experiments under SEM are provided from literature references [10, 15, 20–31] as a func-tion of the investigated surface area in Fig. 1. Spatial resolution varies from one experiment to another and is indicated by the color and size of each dot. Typical resolution using HR-DIC under SEM is below 500 nm to capture the physical deformation mechanisms involved in metallic materials, e.g., deformation slip, deformation twin, or grain boundary sliding. For reference, acquisition times and associated investigated surface areas from relevant studies using optical HR-DIC [28, 32–34] are provided.

To capture deformation events for an area on the order of square millimeters using HR-DIC under SEM, acquisition times can exceed several hours per deformation step, limiting the use of such a technique for high-throughput measurements. The recent development of the multi-beam SEM technology [34] allows for simultaneous acquisition of high-resolution SEM images, yield-ing close to a hundredfold reduction in image acquisition time for a given resolution and field of view. The present technology is used to significantly accelerate HR-DIC measurements using SEM imaging. Variability and sensitivity in HR-DIC measure-ments using the multi-beam technology are evaluated and com-pared to single image acquisition HR-DIC measurements.

Here we demonstrate HR-DIC measurements using the multi-beam SEM technology, which are performed on a nickel-based superalloy to identify the heterogeneity of deformation induced by the grain structure and non-metal-lic inclusions (NMIs) originating from material processing

over an unprecedented field of view. The fatigue resistance of Alloy 718 is susceptible to the characteristics of NMIs and the strain localization in their vicinity [35]. Cracks initiate in the low- and high-cycle fatigue regimes from surface/sub-surface isolated NMIs, clusters of NMIs, or twin boundaries in the vicinity or far from NMIs. It was also observed that NMIs could crack during the first fatigue cycle and induce crack initiation in the matrix later in the fatigue life [35]. NMIs are generally sparsely distributed within the microstructure with a low surface density [35] which makes the investigation of plastic localization and crack initiation at/near NMIs complex. Therefore, sampling very large fields of view at high resolution in a reasonable time for HR-DIC measurements is particularly interesting for such candidate materials. Such a statistical and blind approach is much more suitable to identify microstructural features and configurations prone to crack initiation from NMIs and short crack propagation within the surrounding metallic matrix compared to previous studies investigating and tracking only a few pre-selected NMIs [36]. Moreover, the present unique dataset allows for the identification of rare grain structure features that promote about one order of magnitude higher slip localization amplitude than average. These critical features and associated slip localization events are investigated in detail.

Experimental Characterization

Material and Specimen Preparation

The mechanical specimen was extracted from a wrought polycrystalline nickel-based superalloy Inconel 718 block. The microstructure of the material consists of crystallographic grains with an average grain size of approximately 10 μm, containing annealing twin boundaries, a high γ''-phase content, and a δ-phase content of a few percent. Non-metallic inclusions such as niobium-rich carbides, titanium-rich nitrides, and carbo-nitrides are present and sparsely distributed in the specimen. The nominal composition of the Inconel 718 material is Ni - 0.56%Al - 17.31%Fe - 0.14%Co - 18.0%Cr - 5.4%Nb - 1.00%Ti - 0.023%C - 0.0062%N (wt%). The specimen was machined by electro-discharge machining into a flat, dog bone-shaped geometry. The EDM-affected layer was removed using fine-grit polishing, and the specimen was mirror polished using diamond suspensions down to 1 μm. The specimen was chemical-mechanically polished with 0.05 μm colloidal silica for 24 h. Such a procedure enables electron backscatter diffraction (EBSD) measurements to be performed before deformation. The sample geometry and microstructure of the nickel-based superalloy Inconel 718 are displayed in Figs. 2(a) and 7(b), respectively. Before deformation, a speckle pattern consisting of 60 nm gold nanoparticles was deposited on the surface of the sample, following the pro-cedure by Kammers et al. [17].

Mechanical Testing

The mechanical testing of the specimen was performed using an *in-situ* 5000 Newton tensile stage MT1000 made by NewTec Scientific™. A monotonic tensile test is performed at a quasi-static strain rate of 10^{-3} s^{-1} until a total strain of 1.55% is reached. The macroscopic strain was measured using a strain gauge on the back side of the specimen. After reaching a macroscopic strain of 1.55%, the specimen is unloaded. A residual plastic strain of 0.91% is measured. The images for HR-DIC measurements are performed before loading and after unloading.

Microscopy

Scanning electron imaging was performed in a ThermoFisher™ field emission gun (FEG) Helios600, a Hitachi™ S-4800, and the ZEISS™ MultiSEM 506. The ZEISS™ MultiSEM 506 (MultiSEM) differs from other FEG-SEM models by allowing for the simultaneous acquisi-tion of 91 high-resolution images [37]. An array of electron beams is generated with a micro aperture array illuminated by a single Schottky field emitter. These primary electron beams are then focused by a lens arrangement onto the spec-imen to form a regular pattern of 91 primary electron spots. The bundle of these 91 electron beams is scanned over the sample, and the secondary electron (SE) yield is recorded for each scan position as in any conventional SEM. The SEs that emanate from each primary electron spot are projected via another lens arrangement onto a multi-detector that records all beams simultaneously. SEs are extracted vertically and captured by an upward-acting electric extraction field. Consequently, the SEs generated by individual primary beams can be isolated, providing an undisturbed signal of the cor-responding sub-image [34]. Ninety-one simultaneous images are acquired, and a 5% overlap is used between neighbor-ing images. The 91 simultaneous images form a hexagonal region, referred to as "hexagon" in the present manuscript (see Fig. 2(c)). A single region was investigated using the Helios600 and S-4800 conventional FEGs. However, 577 consecutive hexagons were imaged using the MultiSEM by moving the microscope stage to capture the entire gauge length as shown in Fig. 2. For all microscopes, scanning electron imaging were performed using low acceleration voltage, a beam current of approximately 0.5 nA, an image dwell time of about 0.8 μsec, a horizontal field width of about 12 μm, a working distance of 2 mm for the Helios600 and S-4800 and 1.4 mm for the MultiSEM and a pixel resolution of about 3100 px × 2700 px.

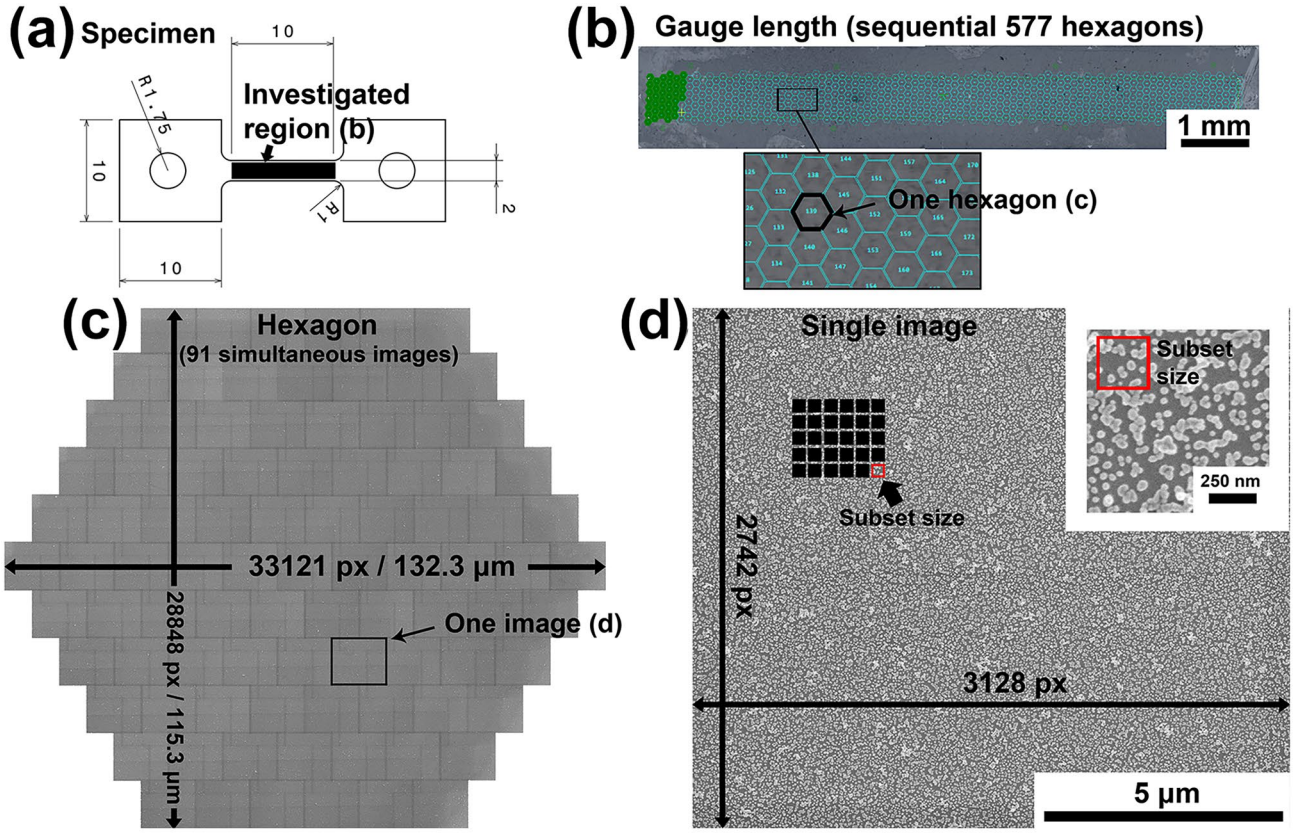

Fig. 2 Investigated region by HR-DIC using the multi-beam technology in the polycrystalline material specimen. **(a)** Geometry of the tensile specimen (dimensions in mm). **(b)** The entire gauge length is imaged using the MultiSEM microscope. The gauge length is imaged using about 550 hexagonal regions (hexagons) of interest that overlap to capture the entire gauge length. **(c)** A hexagon is constituted of 91 independent images acquired simultaneously. (**d**) An image acquired by a single beam using the MultiSEM microscope. The insert displays the speckle pattern used for HR-DIC measurement. The red and black boxes are indicative of the subset size for DIC

Electron Backscatter Diffraction (EBSD) maps were acquired for the investigated regions. EBSD measurements were performed with an EDAX OIM-Hikari XM4 EBSD detector using a step size of 1 µm inside a ThermoFisher™ Scios2. Diffraction patterns were acquired using an accelerating voltage of 30 kV, a 4 × 4 binning, and a beam current of 1 nA. The entire gauge length is captured using EBSD mapping with a 10% overlap between consecutive maps.

Backscatter electron (BSE) imaging was performed using a ThermoFisher™ Axia ChemiSEM using an accelerating voltage of 30 kV, a beam current of 0.6 nA, image dwell time of 10 µsec, and a pixel resolution of 6096 px × 4096 px. The entire gauge length is captured using BSE images with a 10% overlap between consecutive images. The images were stitched using the procedure detailed in the "Data Merging and Segmentation" section.

High-resolution Digital Image Correlation

Images prior to and after deformation were acquired, and the Heaviside-DIC (H-DIC) method was used to extract quantitative measurements of the magnitude of discontinuous displacements over large areas during material deformation. More details are provided elsewhere [7].

During mechanical loading, metals such as the investi-gated nickel-based superalloy develop irreversible plastic-ity that typically manifests in the formation of slip bands. Consequently, slip traces at the free surface of specimens are observed, each associated with a local surface step. This step is produced by dislocations emerging at the surface during plastic deformation by gliding along a crystallographic plane [38]. In-plane displacements occur locally in the material between both sides of the slip trace and can be described by a vector termed "in-plane slip" [7]. The in-plane slip vector

represents the physical in-plane displacement produced by a slip event.

The H-DIC method for the correlation of deformed and undeformed images provides the slip displacement field with regard to the slip trace. Therefore, the full in-plane description of the slip displacements (in-plane slip vector) is obtained from the H-DIC method at every point in the HR-DIC map. The amplitude of the slip is obtained in nanometers for each slip trace with high resolution (less than 10 nm in slip amplitude) [7]. In addition, the slip length and maxi-mum in-plane slip amplitude along the profile of each slip can be extracted.

A subset size of 72 × 72 pixels (287.7 nm × 287.7 nm) with a step size of 9 pixels (35.96 nm) were used for HR-DIC measurements. Examples of subsets are presented in Fig. 2(d).

HR-DIC Measurement by MultiSEM Imaging

Image data were acquired before and after deformation and in total 105,014 image pairs needed to be spatially registered, calling for an automated HR-DIC procedure. The process is described in Fig. 3 and consists of four steps. Initial registration is made between the centers of the hexagons before and after deformation using manually selected control points (sample edges), and a registration algorithm [39] using the package ARGOS (https:// github. com/ charp agne/ Argos_ sampl eScri pts). The resulting dataset is the position of the centers of the hexagons after deformation registered (not accurately) to the position of the centers of the hexagons before deformation, as shown in Fig. 3(Step 1). A higher number of images were acquired after deformation compared to before deformation to capture the entire gauge length. The second step consists of an initial template matching procedure to accurately determine the position of a hexagon before and after deformation to allow comparison to the original state and capture the entire gauge length. The *match template* function of Scikit-image (https:// scikit-image.org/docs/stable/auto_examples/features_ detection/plot_template.html) is used between a region in the center of a given hexagon before deformation and the group of neighbor-ing hexagons after deformation, as shown in Fig. 3(Step 2). The resulting image is a region of the specimen after deforma-tion that includes the region of the investigated hexagon before deformation. The third step consists of the template matching of the 91 images of a given hexagon before deformation with their respective regions after deformation, as shown in Fig. 3(Step 3). The final dataset comprises the registered (at pixel resolution) 91 pairs of images before and after deformation. Processing steps 2 to 4 are repeated for all the hexagons before deforma-tion to obtain the HR-DIC dataset of the entire specimen gauge length. 52,507 pairs of registered images before and after defor-mation are obtained. The final step consists in performing the digital image correlation calculation for all the registered pairs.

A GPU workstation is used to accelerate steps 2 to 4. Massive code parallelization utilizing graphics processing units (GPUs) has been used for the fast computation of vast datasets; this allows for processing each pair of images in seconds. Total processing time was on the order of 600 h.

Data Merging and Segmentation

BSE images and EBSD maps were stitched using the grid stitching algorithm [40] in ImageJ™. In addition, advanced merging algorithms were used to relate deformation slip (HR-DIC measurements) to microstructure (non-metallic

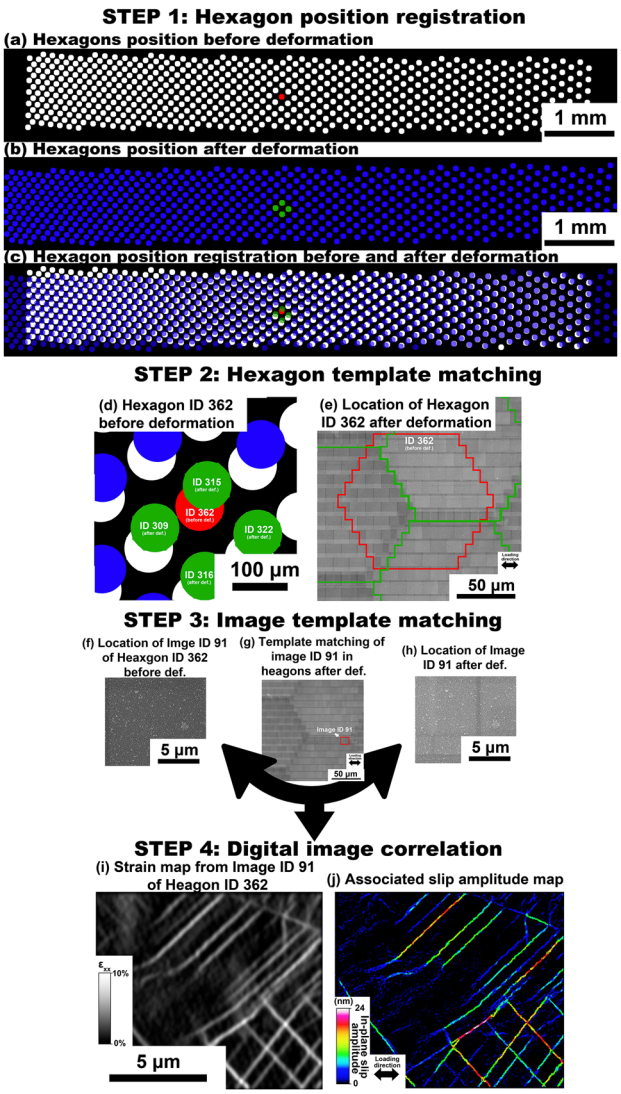

Fig. 3 Procedure for digital image correlation from the MultiSEM imaging. (**Step 1**) Initial registration of the ZEISS™ MultiSEM 506 hexagons centers before and after deformation. (**Step 2**) Extraction of neighboring hexagons after deformation that match a hexagon before deformation. (**Step 3**) Registration of the 91 images that form a hexagon, before and after deformation. (**Step 4**) Digital image correlation to obtain strain fields and slip amplitude maps

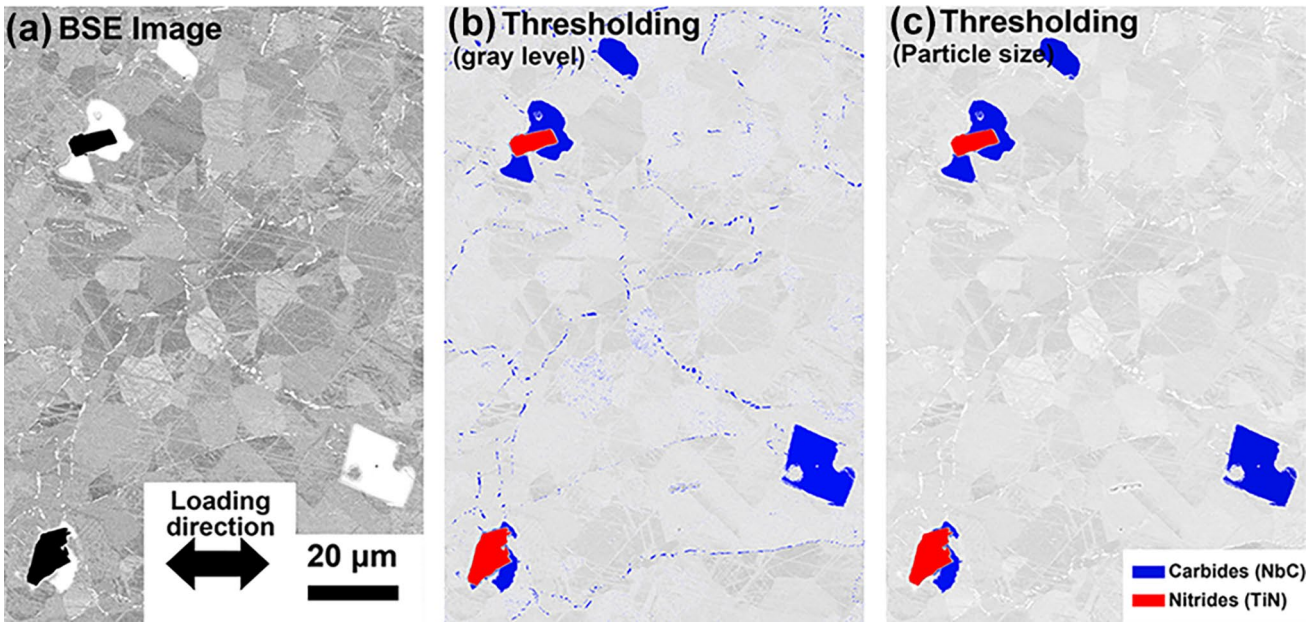

Fig. 4 Data merging and segmentation of the multi-modal dataset. (**a**) Backscatter image of a reduced region of interest displaying non-metallic inclusions. (**b-c**) Subsequent threshold by gray levels and particle size to capture carbide, nitride, and carbonitride inclusions

inclusions (NMI) and crystallographic grains) by HR-DIC, EBSD, and BSE correlative measurements. Details of the merging procedure are provided in ref. [39]. The resulting multimodal dataset consists of large spatially correlated independent maps such as stitched BSE images, inverse pole figure maps, Euler angle maps, strain maps, and slip amplitude maps. In addition, BSE images are thresholds to identify the NMIs, as shown in Fig. 4. Due to differences in Z contrast between the matrix, the NbC carbides, and the TiN nitrides, the identification of NMIs is possible. The first threshold on gray levels (black values) allows segmenta-tion of TiN nitrides, as shown in red in Fig. 4(b). A second threshold on gray levels (white values) allows segmenta-tion of NbC carbides and the δ-phase, as shown in blue in Fig. 4(b). The final threshold using particle size analysis is applied to remove the δ-phase from carbide identification. The NMIs are then classified into four categories: carbides, carbonitrides, clusters of NMIs, and cracked NMIs. While NMIs displayed no cracks before deformation, a fraction cracked during the loading. An NMI is allocated to the cat-egory labeled "cluster of NMIs" if it processes another NMI in the vicinity (less than 20 µm). Carbonitrides are NMIs constituted by carbide(s) and nitride(s). A density of about 150 NMIs per square millimeter was measured.

Results

Variability in HR-DIC Measurements

The variability in HR-DIC measurements is evaluated using the procedure described in refs. [14, 18]. The strain vari-ability is obtained using multiple pairs of images acquired at an identical position without deformation using the image condition described in the previous section. Since the speci-men did not experience deformation, kinematics with only rigid-body motion should be observed. However, drift and spatial distortions, and beam scanning defects generate HR-DIC measurement errors [18, 41]. The standard deviation in ϵ_{xx} (SEM scanning direction / horizontal) and ϵ_{yy} (vertical direction) strains for the different investigated microscopes are provided in Table 1. The standard deviation provided for

Table 1 Standard deviation in HR-DIC measurements and minimum discontinuity amplitude detected as a function of the investigated microscopes

	MultiSEM	Helios600	S-4800
Standard deviation in strain ϵ_{xx}	0.54%	1.31%	1.01%
Standard deviation in strain ϵ_{yy}	0.61%	1.72%	1.58%
Minimum discontinuity amplitude	2.3 nm	3.8 nm	3.1 nm
Standard deviation discontinuity	0.107 nm	0.264 nm	0.204 nm

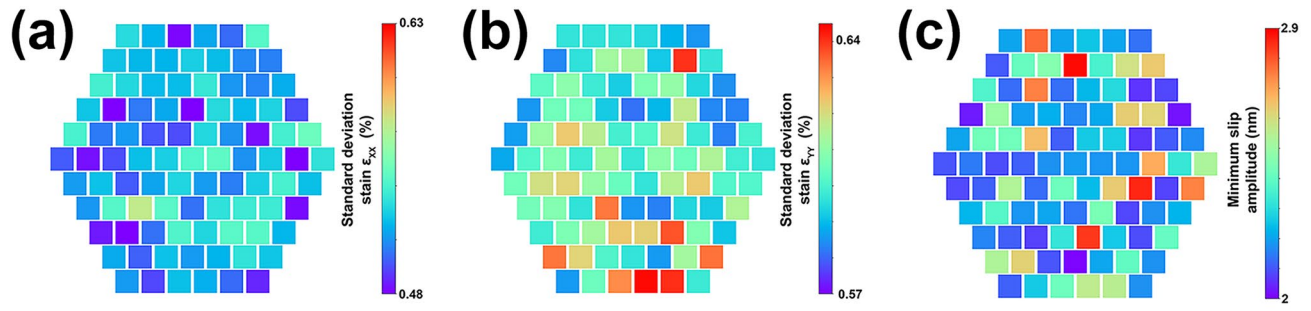

Fig. 5 Standard deviation in HR-DIC measurements and minimum discontinuity amplitude using the MultiSEM between the 91 simultaneous images. **(a)** Standard deviation in ϵ_{xx} (SEM scanning direction / horizontal) strains. **(b)** Standard deviation in ϵ_{yy}. **(c)** Minimum discontinuity amplitude detected

the MultiSEM is the average deviation over the 91 simultaneous pairs of images (one hexagon). The MultiSEM provides HR-DIC measurement variability of at least two times less than other FEG microscopes. The standard deviation in ϵ_{xx} and ϵ_{yy} strains for each of the 91 simultaneous pairs of images using the MultiSEM are provided in Fig. 5(a, b), respectively. Minimum variations in variability are reported from one pair of images to another as a function of the posi-tion in the hexagon.

The minimum slip amplitude detected by the H-DIC method and associated standard deviation is provided in Table 1 for all investigated microscopes. The procedure is described in ref. [14] and consists of using pairs of images between the undeformed and deformed states. The variabil-ity in slip amplitude measurement is associated with beam scanning error and variability in spacing between the dif-ferent SEM scanning lines or scanning points. Better sensi-tivity and lower variability are observed for the MultiSEM

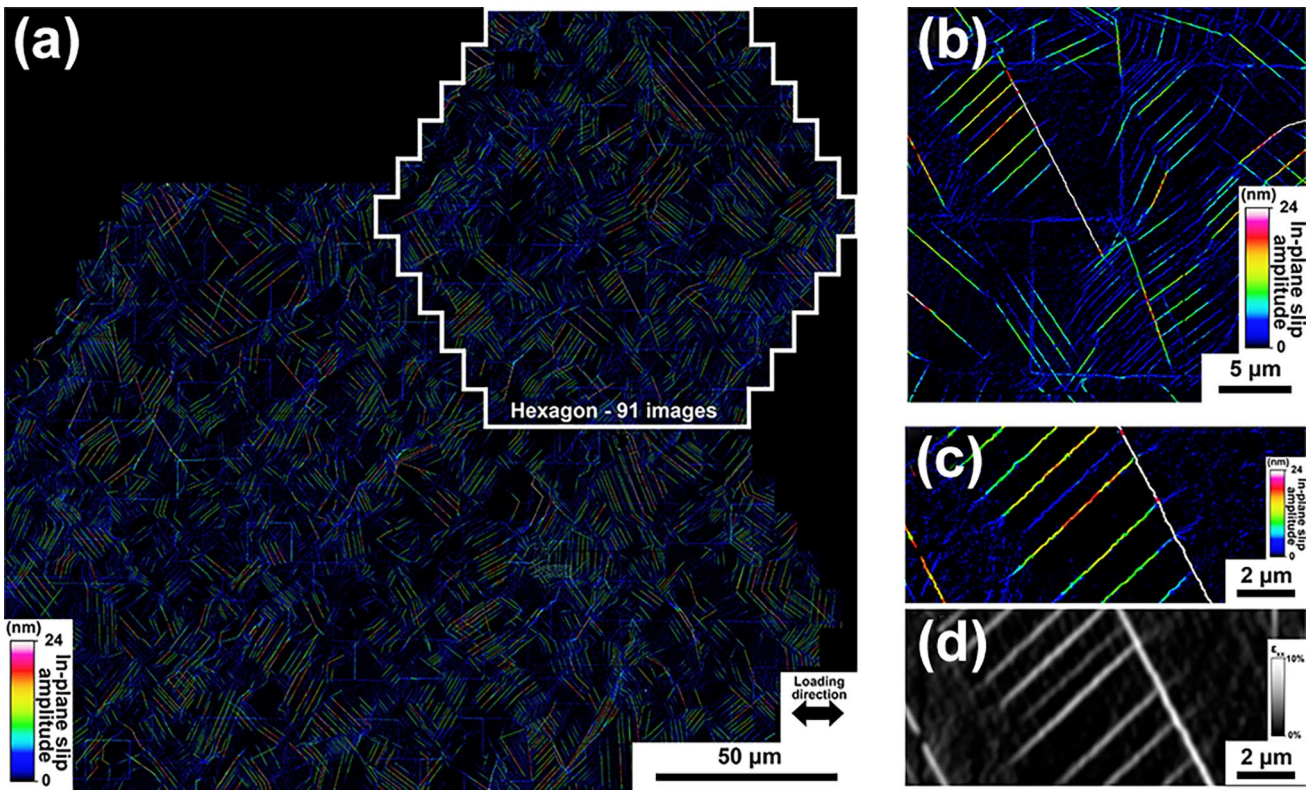

Fig. 6 Slip localization measurement by MultiSEM. **(a)** A reduced region of the slip amplitude map displaying multiple hexagons. Each hexagon is obtained from simultaneous imaging using the MultiSEM and DIC between the undeformed and deformed states. (**b**, **c**, and **d**) High magnification of a reduced region of the slip amplitude and ϵ_{xx} strain maps

compared to the Helios600 and S-4800. The minimum detected slip amplitude for each of the 91 simultaneous pairs of images using the MultiSEM is provided in Fig. 5(c). Minor variations in minimum detected slip amplitude are reported from one pair of images to another as a function of the position in the hexagon.

Slip Localization Measurements

Strains and slip amplitude are captured over the entire gauge length after a macroscopic plastic strain of 0.91%. The HR-DIC dataset consists of 577 hexagons before and after deformation with 105,014 images. H-DIC calcula-tion is performed for every image pair before and after deformation, and the resulting strain and slip amplitude maps are merged using registration from SEM images. The reconstruction for a few hexagons is provided in Fig. 6(a). A reduced region of the slip amplitude and ϵ_{xx} strain maps is provided in Fig. 6(b-d). Bands of concentrated strain are observed on the ϵ_{xx} strain map and are evidence of slip events that develop during deformation. Each of these slip events have amplitudes (given in nanometers) that vary along their profile, as observed on the slip amplitude maps in Fig. 6. The maximum value along the profile is con-sidered and referred to as the maximum slip amplitude. Finally, a large part of the dataset is provided in supple-mentary materials.

Slip Localization in a Nickel-based Superalloy Inconel 718

Over 210,000 slip events were measured over the 7.14 mm^2 investigated region. A large number of slip events randomly selected (300 over the 7.14 mm^2) were investi-gated, and their maximum slip amplitudes were extracted. The distribution of their maximum slip amplitude as a function of the slip length is displayed in Fig. 7(c). In addition, the 50 most intense (highest maximum slip

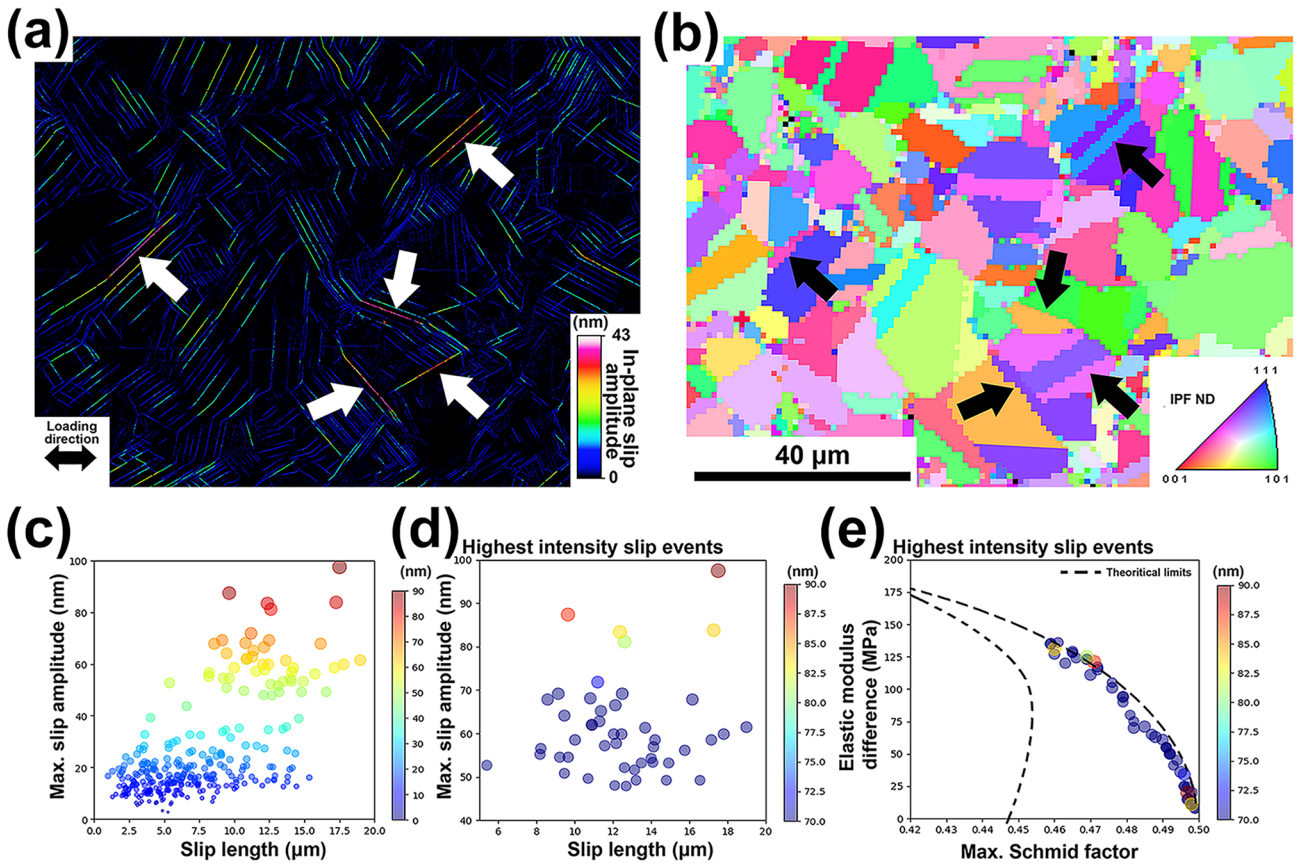

Fig. 7 Intense slip localization near and parallel to twin boundaries in a nickel-based superalloy. **(a)** Slip amplitude map after 0.91% mac-roscopic plastic deformation. **(b)** Associated inverse pole figure map from EBSD measurement. White and black arrows indicate the loca-tion of intense slip events and twin boundaries, respectively. Maximal slip amplitude distribution. **(c)** Maximum slip amplitude of random slip events and of the 50 most intense slip events as a function of their slip length. (**d**) Maximum slip amplitude of the 50 most intense slip events as a function of their slip length. (**e**) Elastic modulus difference and maximum Schmid factor of the twin boundaries associated with the 50 most intense slip events

amplitude) slip events across the entire strain gauge are displayed in Fig. 7(d). The 50 most intense slip events show significantly higher maximum slip amplitude values (about one order of magnitude) than the maximum slip amplitude for the randomly investigated slip events. They also display extended slip length. More importantly, there exist five rare slip events across the entire strain gauge (7.14 mm^2) that display significantly higher slip amplitude than others.

Examples of microstructural configurations that pro-moted the most intense slip events are displayed in Figs. 7 and 10. It is systematically observed that the highest intense slip events are near and parallel to coherent twin boundaries, as indicated by arrows in Figs. 7 and 10. This configuration is referred to in the literature as parallel slip configuration [41]. In addition, the twin boundaries that display intense slip localization amplitude are observed to have an extended length. For each investigated twin boundary associated with the highest maximum slip ampli-tude events, the coherent direction was calculated, and boundaries with the maximum Schmid factor slip system in the coherent {111} plane were identified. These twin boundaries can be described by a combination of a maxi-mum Schmid factor, directional elastic modulus mismatch (between the grains that delimit the twin boundary), and length [41]. Maximum Schmid factor and directional elas-tic modulus are considered along the macroscopic load-ing direction. The Schmid factor and directional elastic modulus of the twin boundaries associated with the high-est maximum slip amplitude are displayed in Fig. 7(c). The theoretical limits [41] between directional elastic modulus and Schmid factor are also reported in Fig. 7(c). As previ-ously observed [41], these boundaries either display a high Schmid factor with a low but existing elastic modulus dif-ference or a relatively low Schmid factor but a significant elastic modulus difference.

Characteristics of the Most Intense Slip Localization Events

The 50 most intense slip events and associated characteristics are investigated in detail. Of the 50 most intense slip events, only three are observed to display direct slip transmission. For the other 47, the slip events are constrained in a single grain. It is observed that these slip events present amplitude profiles along their traces that can be classified into three distinct cat-egories. First, a significant fraction of slip events displays the highest slip amplitude along their profiles in the vicinity of the center of their slip traces. These slip events are referred to as "Type I" and an example is provided in Fig. 8(a) and its

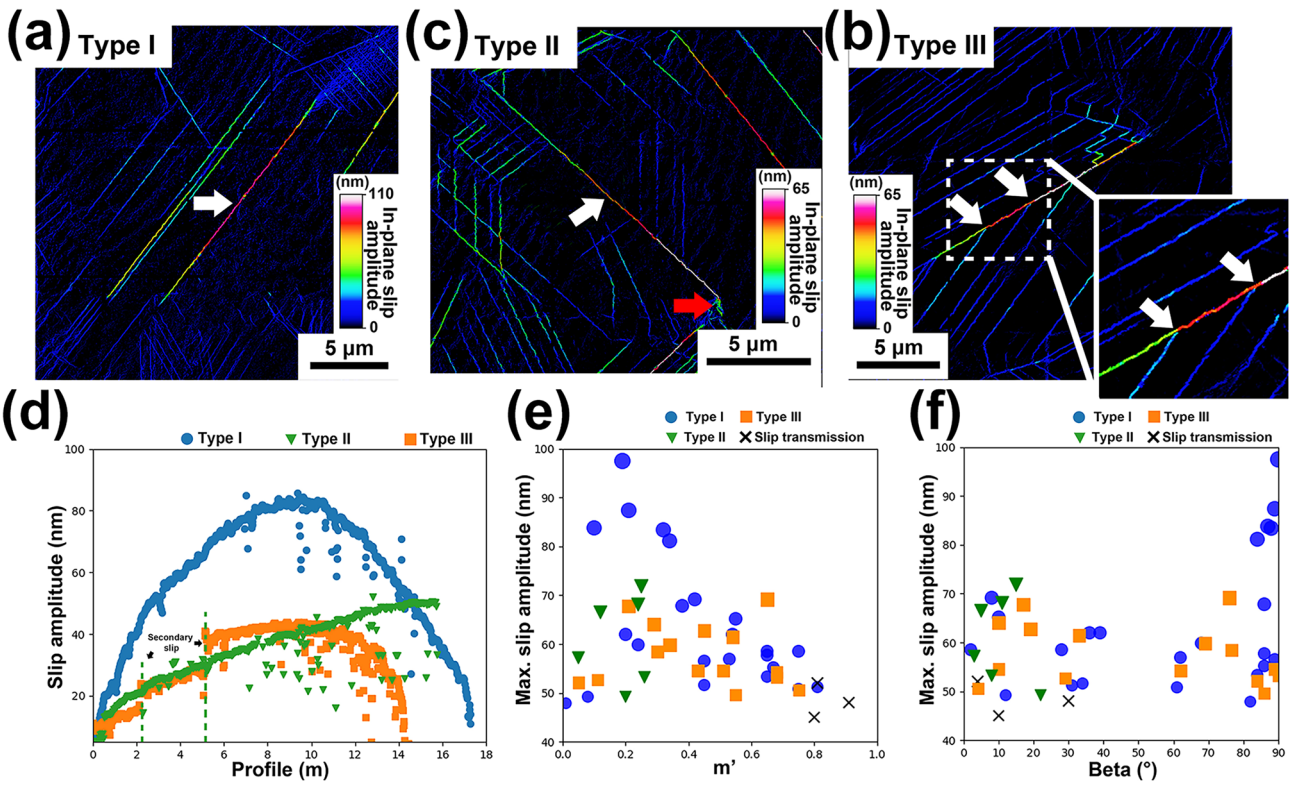

Fig. 8 Slip configuration of the 50 most intense slip events. **(a-c)** Slip amplitude map after 0.91% macroscopic plastic deformation describing the observed three observed types of amplitude profile along slip traces. **(d)** Slip amplitude along slip traces for the observed three observed types of amplitude profile along slip traces. **(e-f)** Maximum slip amplitude of the 50 most intense slip events as a function of the **(e)** m' factor and **(f)** β angle

slip amplitude along its profile displayed in Fig. 8(d). Second, some slip events display a near-constant increase in slip amplitude along their slip trace from one grain boundary to the other one as shown in Fig. 8(b, d). These slip events are referred to as "Type II" in the present paper. Finally, a significant fraction of slip events, referred to as "Type III" display non-continuous amplitude along their profiles as shown in Fig. 8(b). Their slip amplitude along their profiles show different plateaus as presented in the example in Fig. 8(d). Interestingly, secondary slip events are observed where a sudden drop/increase in slip amplitude occurs.

The factor m' = $(d_1.d_2)(n_1.n_2)$ defined by Luster and Morris [42] is employed here to investigate the geometric compatibility between grains and inform non-slip transfer. d_1 and d_2 are the slip directions of the incoming and outgoing slip systems, while n_1 and n_2 are the slip plane normal of the incoming and outgoing slip systems, respectively. High m' values indicate better geometric compatibility between both slip systems. m' factor is calculated for the 50 most intense slip events considering the slip system in neighboring grains that gives the highest m' factor. It is observed in Fig. 8(e) that the five most intense slip events display a low m' factor indicating non-favorable slip transmission. In parallel, the angle β that displays the angle between the slip direction and the direction intersecting the slip plane and specimen surface is presented in Fig. 8(f) for the 50 most intense events. The slip direction is identified using the Heaviside-DIC approach using the method described in ref. [7]. Interestingly, the five most intense slip events identified as Type I display a slip direction out of the specimen surface plane, i.e. free surface. Conversely, the slip events identified as Type II display slip direction near parallel to the specimen surface.

All investigated slip events (50 most intense and 300 slip events randomly selected) were classified as Type I, II, and III, and the histogram of their maximum slip amplitude displayed in Fig. 9 as a function of the type. Slip events that involved slip transmission are not displayed. Interestingly, it is observed that the slip events of Type II only occur for slip amplitude values higher than 45 nm. In contrast, Type I and III slip events appear independently of their slip amplitude.

Role of Non-metallic Inclusions

Some of the intense slip events are located along twin boundaries near NMIs, as shown in Fig. 10(a). The average maximum amplitude of the slip events that occur near carbides, carbonitrides, and clusters of NMIs (about 200 investigated NMIs) or that are not associated with NMI (300 investigated events) are displayed in Fig. 10(b). On average, carbides, carbonitrides, and clusters of NMIs promote slightly higher slip amplitude. The maximum amplitudes of the 50 most intense slip events are displayed in Fig. 10(c)

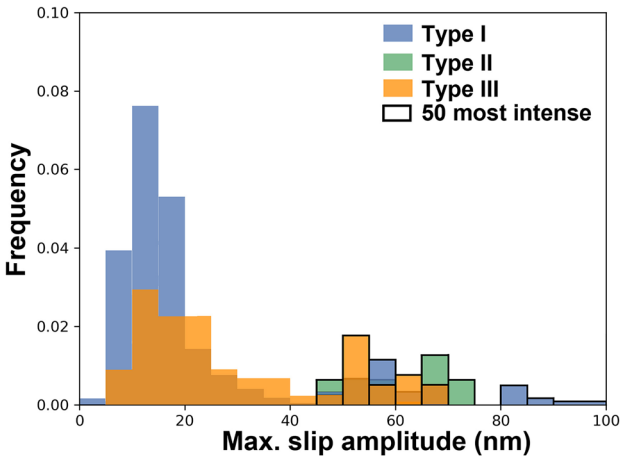

Fig. 9 Slip amplitude profile type for the investigated slip events. The detected slip events are classified as a function of their amplitude pro-file as defined in Fig. 8 and displayed as a function of their maximum slip amplitude

and classified as the function of their location. It is observed that the highest intense slip events are not necessarily occur-ring near NMIs. In addition, the average maximum ampli-tude of the slip events and the maximum amplitudes of the 50 most intense slip events that occur near cracked NMIs are displayed in Fig. 10. The NMIs that show damage dur-ing loading promote slightly higher maximum amplitude in their vicinity on average.

Discussion

Multi-beam SEM Imaging for HR-DIC

The multi-beam technology allows for simultaneous imaging of 91 beams and reduces significantly the required acqui-sition time [34, 37]. In the present study, this technology is used in the MultiSEM microscope to perform HR-DIC measurements. A near hundredfold decrease in acquisition time is obtained, also improving sensitivity and resolution in strain measurements, as shown in Fig. 1, compared to experi-ments with conventional FEG-SEM microscopes. This may be related to the improvement in beam scanning strategy and electronic components used in the MultiSEM micros-copy. Beam scanning artifacts usually control sensitivity and resolution in strain measurements for a given set of DIC parameters [14]. They are not observed using the MultiSEM microscope, as shown in Fig. 5. When using the multi-beam technology, it is important to evaluate if the SEs emanating from each primary electron beam are isolated and provide an undisturbed image signal. While it was previously dem-onstrated for the MultiSEM microscope [34], the obtained

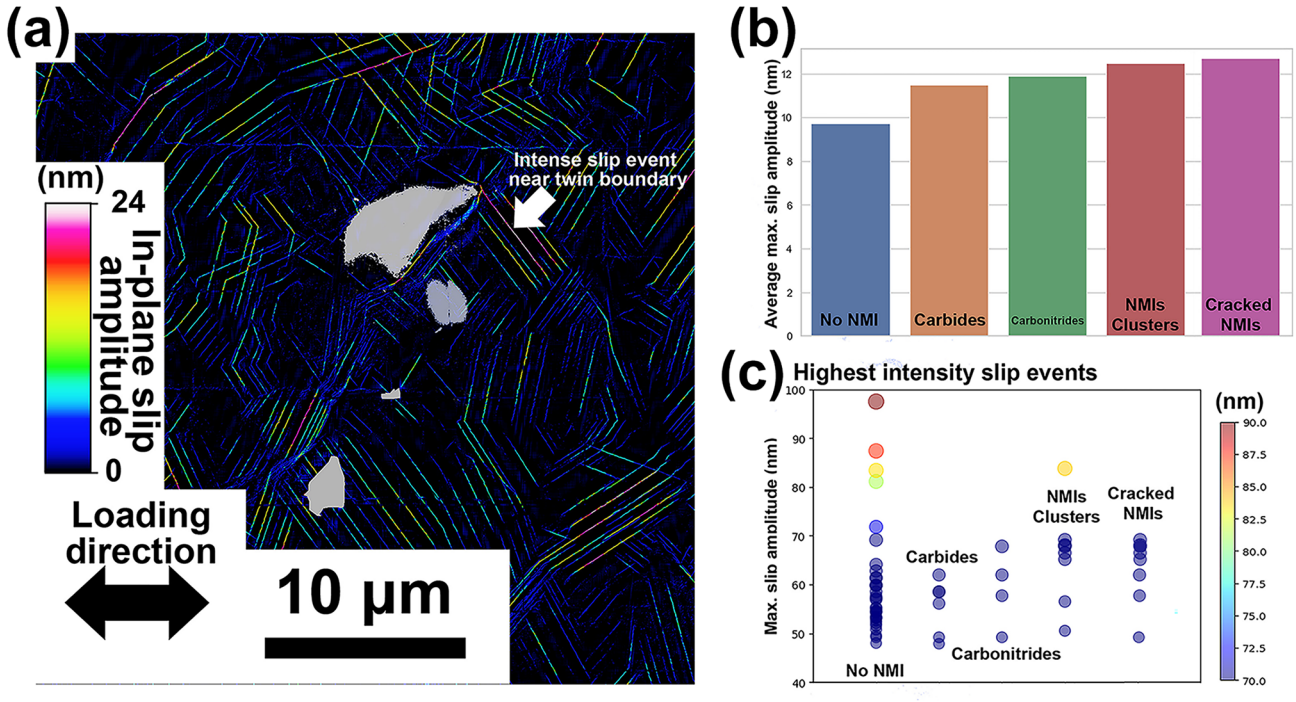

Fig. 10 Effect of NMIs on slip localization. (**a**) Slip amplitude map after 0.91% macroscopic plastic deformation. White regions display carbides. **(b)** Average maximum slip after 0.91% macroscopic plastic deformation for slip events in both the vicinity of NMIs and far from them. **(c)** Average maximum slip after 0.91% macroscopic plastic deformation for the highest intense slip events in both the vicinity of NMIs and far from them

strain sensitivity and resolution also indicate that minimal or nonexistent interaction between emitted SEs from different beams occurs. The acquisition time and investigated surface area for different beam conditions are displayed in Table 2 using a conventional FEG-SEM (Helios600) and the Multi-SEM microscope to give an appreciation for the substantial

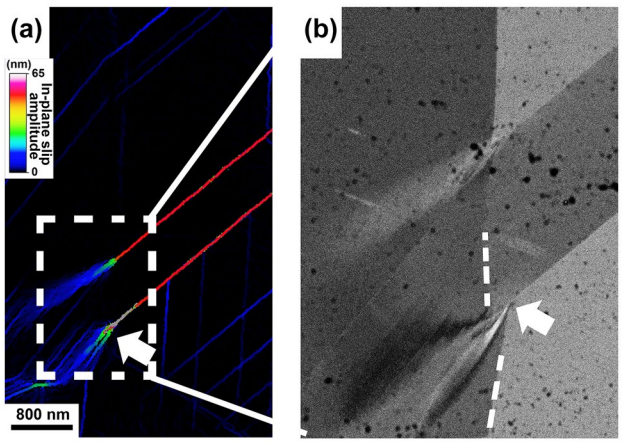

Fig. 11 Grain boundary shearing induced by intense slip localization along twin boundaries. (**a**) Slip amplitude map after 0.91% macroscopic plastic deformation. **(b)** Backscatter electron image of the region displayed in **(a)** by the white box. Dashed lines display the neighboring grain boundary

reduction in acquisition time. Typical HR-DIC measurements (one deformation step) are performed with images with a horizontal field width close to 135 µm and a dwell time of approximately 10 µs [41]. With conventional FEG-SEM, the image acquisition time is almost 3 h for 1mm^2, while only around 2.8 min using the multi-beam technology. The present technology truly upgrades HR-DIC measurements at nanom-eter resolution to high-throughput measurements.

Slip Localization in a Nickel-based Superalloy Inconel 718

Slip localization amplitude in metallic materials was observed to control mechanical properties such as fatigue strength [6], for instance. In nickel-based superalloys, the intense slip events that develop during the first fatigue cycle were observed to induce cracks during cycling [41, 43]. These intense slip events are located near and parallel to twin boundaries that maximize elastic modulus difference across the boundary and Schmid factor [41] and therefore promote the development of high stress/strain concentra-tion during loading [44, 45]. Consequently, fatigue crack nucleation in nickel-based superalloys with a minimum con-tent of metallurgical defects is generally observed to initiate near and parallel to twin boundaries [41]. The present study

Table 2 Acquisition time vs. surface area investigated for conventional FEG microscope and the MultiSEM

	MultiSEM	Conventional FEG-SEM
Image dwell time: 0.8 µs*; HFW:* 12.5 µm*; sensitivity:* 3 nm		
Surface area (577 hexagons)	7.14 mm^2	7.14 mm^2
Acquisition time	65.6 min (1.09 h)	5965.3 min (99.4 h)
Image dwell time: 10 µs*; HFW:* 135 µm*; sensitivity:* 10 nm		
Surface area	1.42 mm^2	1 mm^2
Acquisition time	2.8 min	178.9 min (2.98 h)

HFW refers to the horizontal field width. Sensitivity refers to the minimum discontinuity amplitude that is detectable

identifies the configuration that promotes the most intense localization over an unprecedentedly vast number of twin boundaries. It is observed in Fig. 7(c), as reported in the literature, those twin boundaries that maximize elastic modulus difference and Schmid factor promote the most intense slip localization.

Interestingly, of the more than 210,000 slip events measured over the investigated field of view of 7.14mm^2, only five display slip amplitude values that are significantly higher than the other most intense slip events (see Fig. 7(b)). This indicates that the investigated field of view is insufficient for a representative measurement of these rare events, but this gives credence to the advantages of using multi-beam SEM technology for gathering a high number of statistically sig-nificant data points. As demonstrated in Fig. 1, the conven-tional field of view at high resolution has been constrained to relatively small regions, making these rare events almost certain to be overlooked in most experiments.

These five events display two important characteristics. First, their m' factors are low, indicating geometric incom-patibility with their neighboring grains. Non-slip transmis-sion promotes intense slip localization due to dislocation pileups [46]. Consequently, slip amplitude profiles such as Type I in Fig. 8(d) are observed, as previously reported in literature [46]. More importantly, their slip direction is oriented near 90° to their slip trace (β angle close to 90°). Such slip direction minimizes pileup stresses at grain boundaries facilitating dislocation emergence at the free surface. In the 50 most intense slip events, a large frac-tion displays low β angles as shown in Fig. 8(f). Such configuration favors pileup stresses at grain boundaries, and long-range back-stresses [46, 47]. Interestingly, sev-eral of the highest slip events with low β angles present unusual slip amplitude profiles of Type II (see Fig. 8(d)). Slip amplitude increases progressively up to the grain boundaries, which is inconsistent with pileup behavior, where a zero slip amplitude is expected at boundaries. A high magnification slip amplitude map and associated backscatter electron image at a grain boundary for a Type II slip event are provided in Fig. 11(a, b), respectively. The intense slip events produce a physical shearing of the grain boundary and the occurrence of a so-called microvolume [48, 49]. The grain boundary shears due to intense pileup stresses. Such a mechanism relaxes back-stresses, i.e., slip constraint associated with pileup, and therefore reduces increases in slip amplitude during loading. Consequently, this configuration is not observed to produce the highest slip amplitude. It is also noticed in Fig. 9 that such con-figuration occurs for a maximum slip amplitude exceeding a threshold (here, about 45 nm), and relates to the number of dislocations involved in the pileup at grain boundaries and the grain boundary energy. Interestingly, another mechanism is also shown to decrease slip constraint and therefore slip amplitude as reported for the slip events labeled as Type III in Fig. 8. Secondary slip events reduce slip amplitude along the primary slip events as shown in Fig. 8(d). The previously mentioned mechanisms (grain boundary shearing and secondary slip activation) decrease slip constraint and, therefore, are not associated with the highest slip amplitude.

When metallurgical defects are present, a competitive mechanism occurs between crack nucleation near/at inclu-sions or near twin boundaries far from inclusions [35]. It has been demonstrated that inclusions trigger the development of intense slip localization and consequently form cracks in the vicinity near and parallel to twin boundaries [50]. Identifying the microstructural effect on slip localization is difficult because nanometer resolution and large fields of view are necessary to capture slip localization variability as a function of the microstructure. It is even more challeng-ing when sparsely distributed inclusions are present since a field of view on the order of several square millimeters is necessary to probe a statistically significant number of inclusions. The current approach using multi-beam imaging solves this problem. It is observed in the present study that NMIs, especially clusters of inclusions, promote higher slip localization (see Fig. 10(b)). Clusters of inclusions were pre-viously observed to promote crack initiation in nickel-based superalloy Inconel 718 [35]. The present study highlights the propensity of clusters of inclusions and cracked inclusions to promote intense slip localization. However, the highest slip localization events are not necessarily observed to develop

near NMIs as shown in Fig. 10(c), indicating competition between twin boundaries in the vicinity of and far from NMIs. This competing behavior was also observed when investigating crack initiation in nickel-based superalloy 718 [35] and is now linked to the distribution of the intense slip localization in the vicinity of and far from NMIs.

Conclusions

The present study uses a novel multi-beam SEM technology to reduce image acquisition time drastically and accelerate HR-DIC measurements. The multi-beam SEM technology provides a close to hundredfold acceleration in HR-DIC image acquisition. Variability and resolution in HR-DIC measurements are also improved using multi-beam technology. HR-DIC measurements using this novel SEM technology are performed over an exceptionally large field of view on a nickel-based superalloy to identify the heterogeneity of deformation induced by the grain structure and non-metallic inclusion distribution originating from material processing. Of the over 210,000 slip localization events investigated, the most intense occur near and parallel to twin boundaries, maximizing directional elastic modulus difference and Schmid factor. In addition, non-metallic inclusion clusters and cracked inclusions are observed to promote intense slip localization in their vicinity. A competitive effect of the long favorably-oriented twin boundaries in the vicinity and far from NMIs is observed in the nickel-based superalloy 718. Furthermore, secondary slip activation and grain boundary shearing by intense dislocation pileup are observed to reduce slip amplitude near and parallel to twin boundaries. The most intense slip events are observed to have their slip direction oriented near 90° to their slip trace.

Supplementary Information The online version contains supplementary material available at https://doi.org/10.1007/s11340-023-00961-y.

Acknowledgements R.L.B., C.B., and J.C.S. are grateful for financial support from the Energy & Biosciences Institute (EBI) through the EBI-Shell Program. This work was partly carried out in the Materials Research Laboratory Central Research Facilities, University of Illinois.

Data Availability Data will be made available on request.

Declarations

Conflicts of Interests The authors declare they do not have any known conflicts of interests, financial or personal, regarding this research.

References

1. Stinville JC, Echlin MP, Texier D, Bridier F, Bocher P, Pollock TM (2016) Sub-grain scale digital image correlation by electron microscopy for polycrystalline materials during elastic and plastic deformation. Exp Mech 56(2):197–216. https://doi.org/10.1007/s11340-015-0083-4. (ISSN 1741–2765)
2. Magazzeni CM, Gardner HM, Howe I, Gopon P, Waite JC, Rugg D, Armstrong DEJ, Wilkinson AJ (2021) Nanoindentation in multi-modal map combinations: a correlative approach to local mechanical property assessment. J Mater Res 36(11):2235–2250. https://doi.org/10.1557/s43578-020-00035-y. (ISSN 2044–5326)
3. Wheeler JM, Gan B, Spolenak R (2022) Combinatorial investigation of the ni–ta system via correlated high-speed nanoindentation and edx mapping. Small Methods 6(2):2101084. https://doi.org/10.1002/smtd.202101084
4. Jelinek A, Zak S, Alfreider M, Kiener D (2022) High-throughput micromechanical testing enabled by optimized direct laser writing. Adv Eng Mater 25(7):202200288. https://doi.org/10.1002/adem
5. Ando T (2017) High-speed atomic force microscopy and its future prospects. Biophys Rev 10(2):285–292. https://doi.org/10.1007/s12551-017-0356-5
6. Stinville JC, Charpagne MC, Cervellon A, Hemery S, Wang F, Callahan PG, Valle V, Pollock TM (2022) On the origins of fatigue strength in crystalline metallic materials. Science 377(6610):1065–1071
7. Bourdin F, Stinville JC, Echlin MP, Callahan PG, Lenthe WC, Torbet CJ, Texier D, Bridier F, Cormier J, Villechaise P, Pollock TM, Valle V (2018) Measurements of plastic localization by heaviside-digital image correlation. Acta Mater 157:307–325. https://doi.org/10.1016/j.actamat.2018.07.013. (ISSN 1359–6454)
8. Chen Z, Lenthe W, Stinville JC, Echlin M, Pollock TM, Daly S (2018) High-resolution deformation mapping across large fields of view using scanning electron microscopy and digital image correlation. Exp Mech 58(9):1407–1421. https://doi.org/10.1007/s11340-018-0419-y. (ISSN 1741–2765)
9. Jiang R, Pierron F, Octaviani S, Reed PAS (2017) Characterisation of strain localisation processes during fatigue crack initiation and early crack propagation by sem-dic in an advanced disc alloy. Mater Sci Eng A 699:128–144. https://doi.org/10.1016/j.msea.2017.05.091. (ISSN 0921–5093)
10. Edwards TEJ, Di Gioacchino F, Clegg WJ (2021) High resolution digital image correlation mapping of strain localization upon room and high temperature, high cycle fatigue of a tial intermetallic alloy. Int J Fatigue 142:105905. https://doi.org/10.1016/j.ijfatigue.2020.105905. (ISSN 0142–1123)
11. Mello AW, Nicolas A, Sangid MD (2017) Fatigue strain mapping via digital image correlation for ni-based superalloys: the role of thermal activation on cube slip. Mater Sci Eng A 695:332–341. https://doi.org/10.1016/j.msea.2017.04.002. (ISSN 0921–5093)
12. Xu X, Lunt D, Thomas R, Prasath Babu R, Harte A, Atkinson M, da Fonseca JQ, Preuss M (2019) Identification of active slip mode in a hexagonal material by correlative scanning electron microscopy. Acta Mater 175:376–393. https://doi.org/10.1016/j.actamat.2019.06.024. (ISSN 1359–6454)
13. Sperry R, Han S, Chen Z, Daly SH, Crimp MA, Fullwood DT (2021) Comparison of ebsd, dic, afm, and ecci for active slip system identification in deformed ti-7al. Mater Charact 173:110941. https://doi.org/10.1016/j.matchar.2021.110941. (ISSN 1044–5803)
14. Stinville JC, Francis T, Polonsky AT, Torbet CJ, Charpagne MA, Chen Z, Balbus GH, Bourdin F, Valle V, Callahan PG, Echlin MP, Pollock TM (2021) Time-resolved digital image correlation in the scanning electron microscope for analysis of time-dependent mechanisms. Exp Mech 61(2):331–348. https://doi.org/10.1007/s11340-020-00632-2. (ISSN 17412765)
15. Montgomery CB, Koohbor B, Sottos NR (2019) A robust patterning technique for electron microscopy-based digital image

correlation at sub-micron resolutions. Exp Mech 59(7):1063–1073. https://doi.org/10.1007/s11340-019-00487-2
16. Hoefnagels JPM, van Maris MPFHL, Vermeij T (2019) One-step deposition of nano-to-micron-scalable, high-quality digital image correlation patterns for high-strainiin-situ/imulti-microscopy testing. Strain 55(6):e12330. https://doi.org/10.1111/str.12330
17. Kammers AD, Daly S (2013) Self-assembled nanoparticle surface patterning for improved digital image correlation in a scanning electron microscope. Exp Mech 53(8):1333–1341. https://doi.org/10.1007/s11340-013-9734-5. (ISSN 0014–4851)
18. Kammers AD, Daly S (2013) Digital image correlation under scanning electron microscopy: Methodology and validation. Exp Mech 53(9):1743–1761. https://doi.org/10.1007/s11340-013-9782-x. (ISSN 0014–4851)
19. Chen Z, Daly S (2018) Deformation twin identification in magnesium through clustering and computer vision. Mater Sci Eng A 736:61–75. https://doi.org/10.1016/j.msea.2018.08.083. (ISSN 0921–5093)
20. Mansouri Arani M, Ramesh NS, Wang X, Parson N, Li M, Poole WJ (2022) The localization of plastic deformation in the precipitate free zone of an al-mg-si-mn alloy. Acta Mater 231:117872. https://doi.org/10.1016/j.actamat.2022.117872. (ISSN 1359–6454)
21. Atkinson MD, Donoghue JM, da Fonseca JQ (2020) Measurement of local plastic strain during uniaxial reversed loading of nickel alloy 625. Mater Charact 168:110561. https://doi.org/10.1016/j.matchar.2020.110561. (ISSN 1044–5803)
22. Harr ME, Daly S, Pilchak AL (2021) The effect of temperature on slip in microtextured ti-6al-2sn-4zr-2mo under dwell fatigue. Int J Fatigue 147:106173. https://doi.org/10.1016/j.ijfatigue.2021.106173. (ISSN 0142–1123)
23. Linne MA, Bieler TR, Daly S (2020) The effect of microstructure on the relationship between grain boundary sliding and slip transmission in high purity aluminum. Int J Plast 135:102818. https://doi.org/10.1016/j.ijplas.2020.102818. (ISSN 0749–6419)
24. Rotella J, Mello AW, Venkataraman A, Buckingham R, Hardy M, Sangid MD (2021) Dwellfatigue of ni-based superalloys with serrated and planar grain boundary morphologies: yhe role of the γ phase on strain accumulation and cavitation. Metall Mater Trans A 52(11):5079–5095. https:// doi. org/ 10. 1007/ s11661- 021- 06454-
8. (ISSN 1543–1940)
25. Weidner A, Biermann H (2021) Review on strain localization phenomena studied by high-resolution digital image correlation. Adv Eng Mater 23(4):2001409. https://doi.org/10.1002/adem.202001409
26. Vermeij T, Hoefnagels JPM (2022) Plasticity, localization, and damage in ferritic-pearlitic steel studied by nanoscale digital image correlation. Scr Mater 208:114327. https://doi.org/10.1016/j.scriptamat.2021. (ISSN 1359–6462)
27. Carroll J, Abuzaid W, Lambros J, Sehitoglu H (2010) An experimental methodology to relate local strain to microstructural texture. Rev Sci Inst 81(8):083703. https://doi.org/10.1063/1.3474902
28. Guery A, Hild F, Latourte F, Roux S (2016) Slip activities in polycrystals determined by coupling dic measurements with crystal plasticity calculations. Int J Plast 81:249–266. https://doi.org/10.1016/j.ijplas.2016.01.008. (ISSN 0749–6419)
29. Wang X, Pan Z, Fan F, Wang J, Liu Y, Mao SX, Zhu T, Xia S (2015) Nanoscale deformation analysis with high-resolution trans-mission electron microscopy and digital image correlation. J Appl Mech 82(12):121001. https://doi.org/10.1115/1.4031332. (ISSN 0021–8936)
30. Zhang Y, Feng L, Dillon S, Lambros J (2022) Full-field deformation measurements in the transmission electron microscope using digital image correlation and particle tracking. Mater Charact 183:111598. https://doi.org/10.1016/j.matchar.2021.111598. (ISSN 1044–5803)
31. Carroll JD, Abuzaid W, Lambros J, Sehitoglu H (2013) High resolution digital image correlation measurements of strain accumulation in fatigue crack growth. Int J Fatigue 57:140–150. https://doi.org/10.1016/j.ijfatigue.2012.06.010. (ISSN 0142–1123; Fatigue and Microstructure: A special issue on recent advances)
32. Abuzaid WZ, Sangid MD, Carroll JD, Sehitoglu H, Lambros J (2012) Slip transfer and plastic strain accumulation across grain boundaries in hastelloy x. J Mech Phys Solids 60(6):1201–1220. https://doi.org/10.1016/j.jmps.2012.02.001. (ISSN 0022–5096)
33. Bertin M, Du C, Hoefnagels JPM, Hild F (2016) Crystal plasticity parameter identification with 3d measurements and integrated digital image correlation. Acta Mater 116:321–331. https://doi.org/10.1016/j.actamat.2016.06.039. (ISSN 1359–6454)
34. Keller AL, Zeidler D, Kemen T (2014) High throughput data acquisition with a multi-beam SEM. In: Postek MT, Newbury DE, Frank Platek S, Maugel TK (eds) SPIE Proceedings. SPIE. https://doi.org/10.1117/12.2069119
35. Texier D, Stinville JC, Echlin MP, Pierret S, Villechaise P, Pollock TM, Cormier J (2019) Short crack propagation from cracked non-metallic inclusions in a ni-based polycrystalline superalloy. Acta Mater 165:241–258. https://doi.org/10.1016/j.actamat.2018.11.051.(ISSN 1359–6454)
36. Texier D, Stinville JC, Charpagne MA, Chen Z, Valle V, Villechaise P, Pollock TM, Cormier J (2020) Role of non-metallic inclusions and twins on the variability in fatigue life in alloy 718 nickel base superalloy. In: Tin S, Hardy M, Clews J, Cormier J, Feng Q, Marcin J, O'Brien C, Suzuki A (eds) Superalloys. Springer International Publishing, Cham, pp 629–639 (ISBN 978–3–030–51834–9)
37. Marx V (2013) Brain mapping in high resolution. Nature 503(7474):147–152. https://doi.org/10.1038/503147a. (ISSN 1476–4687)
38. Hull D, Bacon DJ (2011) Introduction to dislocations. Materials science and technology. Elsevier Science (ISBN 9780080966731)
39. Charpagne MA, Strub F, Pollock TM (2019) Accurate reconstruction of ebsd datasets by a multimodal data approach using an evolutionary algorithm. Mater Charact 150:184–198. https://doi.org/10.1016/j.matchar.2019.01.033. (ISSN 1044–5803)
40. Preibisch S, Saalfeld S, Tomancak P (2009) Globally optimal stitching of tiled 3d microscopic image acquisitions. Bioinformatics 25(11):1463–1465. https://doi.org/10.1093/bioinformatics/btp184. (ISSN 1367–4811)
41. Stinville JC, Martin E, Karadge M, Ismonov S, Soare M, Hanlon T, Sundaram S, Echlin MP, Callahan PG, Lenthe WC, Miller VM, Miao J, Wessman AE, Finlay R, Loghin A, Marte J, Pollock TM (2018) Fatigue deformation in a polycrystalline nickel base superalloy at intermediate and high temperature: competing failure modes. Acta Mater 152:16–33. https://doi.org/10.1016/j.actamat.2018.03.35. (ISSN 1359–6454)
42. Luster J, Morris MA (1995) Compatibility of deformation in two-phase ti-al alloys: dependence on microstructure and orientation relationships. Metall Mater Trans A 26(7):1745–1756. https://doi.org/10.1007/BF02670762. (Cited by: 266)
43. Mughrabi H (2013) Cyclic slip irreversibility and fatigue life: a microstructure-based analysis. Acta Mater 61(4):1197–1203. https://doi.org/10.1016/j.actamat.2012.10.029. (ISSN 1359–6454)
44. Pinz M, Weber G, Stinville JC, Pollock T, Ghosh S (2022) Data-driven bayesian model-based prediction of fatigue crack nucleation in ni-based superalloys. npj Comput Mater 8(1):39. https://doi.org/10.1038/s41524-022-00727-5. (ISSN 2057–3960)
45. Zhang X, Stinville JC, Pollock TM, Dunne FPE (2021) Crystallography and elastic anisotropy in fatigue crack nucleation at nickel alloy twin boundaries. J Mech Phys Solids 155:104538. https://doi.org/10.1016/j.jmps.2021.104538. (ISSN 0022–5096)
46. Sperry R, Harte A, da Fonseca JQ, Homer ER, Wagoner RH, Fullwood DT (2020) Slip band characteristics in the presence of grain boundaries

in nickel-based superalloy. Acta Mater 193:229–238. https://doi.org/10.1016/j.actamat.2020.04.037. (ISSN 1359–6454)
47. Hirth JP, Lothe J, Mura T (1983) Theory of dislocations (2nd ed.). J Appl Mech 50(2):476–477. https://doi.org/10.1115/1.3167075. (ISSN 0021–8936)
48. Villechaise P, Cormier J, Billot T, Mendez J (2012) Mechanical behaviour and damage processes of Udimet 720Li: influence of localized plasticity at grain boundaries. 12th International Symposium on Superalloys, pp 15–24
49. Larrouy B, Villechaise P, Cormier J, Berteaux O (2015) Grain boundary–slip bands interactions: impact on the fatigue crack initiation in a polycrystalline forged ni-based superalloy. Acta Mater 99:325–336. https://doi.org/10.1016/j.actamat.2015.08.9. (ISSN 1359–6454)
50. Bergsmo A, Xu Y, Poole B, Dunne FPE (2022) Twin boundary fatigue crack nucleation in a polycrystalline nickel superalloy containing non-metallic inclusions. J Mech Phys Solids 160:104785. https://doi.org/10.1016/j.jmps.2022.104785. (ISSN 0022–5096)